WILEY

Modeling of multicomponent diffusions and natural convection in unfractured and fractured media by discontinuous Galerkin and mixed methods

Hussein Hoteit[1] | Abbas Firoozabadi[2,3]

[1]Physical Science and Engineering Division, King Abdullah University of Science and Technology, Thuwal, Saudi Arabia

[2]Reservoir Engineering Research Institute, Palo Alto, California, USA

[3]School of Engineering and Applied Science, Yale University, New Haven, Connecticut, USA

Correspondence

Hussein Hoteit, Physical Science and Engineering Division, King Abdullah University of Science and Technology, Thuwal 23955-6900, Saudi Arabia.
Email: hussein.hoteit@kaust.edu.sa

Summary

Computation of the distribution of species in hydrocarbon reservoirs from diffusions (thermal, molecular, and pressure) and natural convection is an important step in reservoir initialization. Current methods, which are mainly based on the conventional finite-difference approach, may not be numerically efficient in fractured and other media with complex heterogeneities. In this work, the discontinuous Galerkin (DG) method combined with the mixed finite element (MFE) method is used for the calculation of compositional variation in fractured hydrocarbon reservoirs. The use of unstructured gridding allows efficient computations for fractured media when the cross flow equilibrium concept is invoked. The DG method has less numerical dispersion than the upwind finite-difference methods. The MFE method ensures continuity of fluxes at the interface of the grid elements. We also use the local DG (LDG) method instead of the MFE to calculate the diffusion fluxes. Results from several numerical examples are presented to demonstrate the efficiency, robustness, and accuracy of the model. Various features of convection and diffusion in homogeneous, layered, and fractured media are also discussed.

KEYWORDS

compositional modeling, convection-diffusion flow equations, discontinuous Galerkin method, discrete fracture model, fractured porous media, mixed finite element method

1 | INTRODUCTION

Many reservoirs around the world exhibit compositional variations, vertically and laterally.[1-3] These gradients can significantly affect the hydrocarbon characteristics such as the API gravity, producing gas-oil ratio (GOR), saturation pressure, and the total hydrocarbons in place. Reservoir fluid initialization has a major impact on reservoir production predictions. The number and location of offshore wells are critically related to the distribution of species in the subsurface formation. For instance, Metcalfe et al[4] reported significant compositional gradients in the Anschutz Ranch East field, which resulted in different gas-oil-ratio behaviors observed at different wells in the field. In a big reservoir (43 km long, 23 km wide) in the Middle East, Hamoodi et al[5] observed large compositional variations in the areal extent. Some components showed 10-fold difference in composition across the reservoir. Similar phenomena have also been observed in many other fields.[6-10] There are 3 distinct processes that affect species distribution in hydrocarbon reservoirs. These include (i) natural convection, (ii) different diffusion mechanisms, and (iii) reservoir filling and leakage.[11] Natural convection is mainly affected

by horizontal temperature gradient. Diffusions are from temperature, pressure, and composition gradients. Reservoir filling and leakage are from the sources outside the reservoir domain. Current practice in reservoir engineering is mainly based on 1-dimensional (1D) vertical variation in composition with depth due to gravity and thermal gradients.[12,13] Horizontal species distribution is often ignored in the reservoir. When there is no reservoir filling and leakage, compositional variations in connected hydrocarbon reservoirs are mainly from natural convection and Fickian, pressure, and thermal diffusions. There are only a few studies in the literature that incorporate the effect of diffusions and natural convection on hydrocarbon species distribution. Jacqmin[14] investigated the compositional variation in homogeneous porous media in accounting for natural convection and Fickian diffusion in a binary mixture. Riley and Firoozabadi[15] studied the effect of the thermal, pressure, and Fickian diffusion as well as natural convection for a single-phase 2-component fluid in a homogeneous cross-sectional reservoir with a given linear temperature distribution. For a methane (C_1/normal) butane (nC_4) binary mixture, they reported that methane segregates toward the bottom-hot side of the domain. They also showed that a small amount of convection could cause the horizontal composition gradient to increase until a certain limit, which varies with permeability. They solved the steady-state mass conservation equation and Darcy's law using a successive iteration approach based on Poisson's equation.[15] This method is accurate in approximating the horizontal compositional variation. However, the convergence rate is slow, and therefore, it is computationally costly at high permeabilities. Ghorayeb and Firoozabadi[16,17] used the finite-difference (FD) method to investigate the diffusion and convection effects in multicomponent mixtures in homogeneous 2-dimensional (2D) rectangular domains. In their implementation, the steady-state solution was obtained by solving the unsteady-state equations and iterating on time until reaching convergence. They found that, unlike in binary hydrocarbons, methane in ternary or multicomponent mixtures can get to a higher concentration at the cold top-side in a rectangular domain. Subsequently, Ghorayeb and Firoozabadi[18] used the same numerical approach to approximate the multicomponent diffusion and convection in a fractured rectangular domain. A uniform network of connected and disconnected fractures was considered using a single-porosity model. Because of the length-scale and permeability contrasts between the matrix and the fracture grid cells, the numerical discretization gave rise to large and ill-conditioned linear systems. For a 30 m × 15 m fractured cross-section with a 1-mm fracture aperture, a grid of about 45 000 elements was required. Consequently, this approach may not be practical for compositional variation calculations in fractured reservoirs of more realistic geometrical dimensions.

Ghorayeb and Firoozabadi[16-18] assumed that the Oberbeck-Boussinesq approximation was valid for a limited range of temperature, pressure, and composition. In this work, we consider the unsteady-state convection-diffusion flow equations without Oberbeck-Boussinesq assumption. The fluid density is calculated using the Peng-Robenson equation of state (PR-EOS). Our requirements for the numerical solution of the flow equations are (i) mass is conserved locally at the cell level, (ii) numerical dispersion is low enough to study physical dispersion/diffusion, and (iii) unstructured grids are used to provide flexibility to describe complicated geometries including fractures. In previous studies,[19-21] we provided a detailed description of the numerical approach in approximating pure convective multicomponent flow equations in fractured media. The discontinuous Galerkin (DG) method was used to solve the convection-diffusion equations. The FD method has poor accuracy on unstructured grids and lacks the flexibility to describe complicated geometries. Our objective is to develop an accurate and efficient numerical method for calculating the compositional variation of multicomponent mixtures, taking into account the diffusions and natural convection processes in homogeneous and fractured media with connected and disconnected fractures.

Numerical approximations based on cell-centered finite volume (FV) methods compute the surface integrals (convection and diffusion fluxes) at the cell boundaries. Russell and Wheeler[22] showed that the mixed finite element (MFE) method, with a surface integration formula, becomes equivalent to the FD method on structured grids (see also the work of Chavent and Roberts[23]). The formulation was used by Weiser and Wheeler[24] to develop optimal convergence for both pressure and velocity in cell-centered FD methods in rectangular grids. Arbogast et al[25,26] extended this formulation to full tensors in triangular and logically rectangular grids. In distorted quadrilaterals and hexahedra, a multipoint flux MFE method was later developed by Wheeler et al.[27,28] For unstructured grids, the MFE method is superior to the conventional finite element and FV methods in terms of flux accuracy, particularly with a strong discontinuity in the transmissivity.[29,30] In this study, we use the MFE method with the lowest-order Raviart-Thomas space.[31] The main features of the MFE method are (i) the pressure and fluxes are approximated simultaneously with the same order of convergence and (ii) a locally conservative method suitable to model full permeability tensors. The MFE method may produce ill-conditioned linear systems where the cell pressure averages and the interelement fluxes are the primary unknowns. To overcome this issue, we use the hybridized MFE technique,[32-34] where the primary unknowns are the edge pressure averages (pressure traces). In this paper, we refer to the hybridized MFE method by the MFE method.

With natural convection, the magnitude of the flow velocity is relatively very small (in the order of 10^{-10} m/s) compared to the case when the field is under primary or secondary depletion. We found that high accuracy in approximating the

convective fluxes is needed to capture the convective fluid circulations in the reservoir. We provide a numerical example showing that the calculation of natural convective velocity by the standard 2-point FD approximation leads to inaccuracy in the velocity field in heterogeneous media. Therefore, we recommend using the MFE method. One drawback of the MFE method in calculating the diffusion fluxes is the size of the linear system, which is equal to the number of the mesh edges. To overcome this difficulty, an alternative approach is to use the local DG (LDG) method. Other authors coupled the DG and MFE methods[35-37] for similar applications.

This work provides an original contribution to the numerical modeling of muticomponent fluid flow in fractured media in the context of natural convection and diffusions. The main new contributions can be summarized in 2 aspects. (i) We investigated the impact of reservoir heterogeneity and fractures with unstructured distribution on the fluid flow circulation and hydrocarbon compositional variation in a reservoir from natural convection and diffusions. (ii) We proposed a numerical approach that combines the MFE and LDG methods to solve the convection-diffusion equations, where diffusions are described by a full diffusion tensor that is a function of pressure, temperature, and composition.

The LDG method was first introduced by Cockburn and Shu[38] as an extension of the DG method to approximate the convection-diffusion equation. This method is similar to the MFE method concerning the flux calculation; the primary unknown and its gradient are approximated simultaneously. Unlike the MFE method, the LDG method allows a local evaluation of the diffusion fluxes. However, we demonstrate that the MFE method is more accurate in approximating the diffusion fluxes in nonsmooth finite element grids.

In this study, we use the concept of cross flow equilibrium to represent a flow in fractured media. The model based on this concept has been referred to as "the discrete fracture model" and is an alternative to the single- or dual-porosity model. It can be used to describe connected and disconnected fractures. Because the fracture aperture is very small compared to the matrix size, this approach allows us to represent the fractures using 1D linear elements within a 2D system.[39,40] Thus, a fracture entity can be logically represented by the cell edges. This simplification of the fractures reduces significantly the computational requirements. We use the MFE method to approximate the pressure and the velocity in the fractures. As a result, the fluxes at the intersection of multifractures are correctly calculated. In this paper, we first present a mathematical model describing the convection-diffusion flow of multicomponent fluids; we then briefly describe the numerical model that combines the MFE and DG methods. Convection and diffusion fluxes are approximated by both the MFE and LDG methods. We present numerical examples comparing the MFE and the 2-point FD methods for the convection fluxes with the MFE and LDG methods for the diffusion fluxes. To demonstrate the efficiency and robustness of our numerical approach, we provide examples that cover homogeneous, heterogeneous, and fractured media.

2 | MATHEMATICAL MODEL

We consider a single-phase system with n_c components. For each component i, the mass balance is expressed by the following convection-diffusion equation:

$$\phi \frac{\partial z_i c}{\partial t} + \nabla.(z_i c \vartheta) + \nabla.\boldsymbol{J}_i = 0 \quad i = 1, \dots, n_c \quad \text{in} \quad \Omega \times (0, \tau),$$ (1)

where ϕ is the porosity, c is the molar density, z_i is the mole fraction of component i, $\boldsymbol{J}_i$ is the molar diffusion flux of component i, Ω is the 2D computational domain, and τ denotes the simulation time.

The bulk velocity field ϑ is given by Darcy's law

$$\vartheta = -\frac{\boldsymbol{k}}{\mu}(\nabla p - \rho \boldsymbol{g}) \quad \text{in} \quad \Omega \times (0, \tau),$$ (2)

where $\boldsymbol{k}$ is the absolute permeability tensor and μ, p, and ρ are the viscosity, pressure, and mass density, respectively. The gravitational constant vector $\boldsymbol{g}$ is oriented downward.

The flow Equations 1 and 2 are coupled with the PR-EOS that models the density as a function of composition, temperature, and pressure

$$\begin{cases} \rho = cM, \\ c = \frac{p}{ZRT}, \\ Z^3 - (1-B)Z^2 + (A - 3B^2 - 2B)Z - (AB - B^2 - B^3) = 0, \end{cases}$$ (3)

where M is the molecular weight, R is the gas constant, T is the temperature, and A and B are the PR-EOS parameters.[41,42]

Ghorayeb and Firoozabadi[43] expressed the diffusion mass flux $\boldsymbol{J}_i$ in a single-phase mixture in the general form

$$\boldsymbol{J}_i = -c \left(\sum_{j=1}^{n_c-1} D_{ij}^M \nabla z_j + D_i^p \nabla p + D_i^T \nabla T \right), \qquad (4)$$

where D_{ij}^M, D_i^p, and D_i^T are, respectively, the coefficients of the molecular diffusion between components i and j, pressure diffusion, and thermal diffusion. Details of the diffusion coefficients are provided in the works of Ghorayeb and Firoozabadi[43] and Firoozabadi et al.[44] Summing up Equation 1 over all components and using the facts that $\sum_{i=1}^{n_c} z_i = 1$ and $\sum_{i=1}^{n_c} \boldsymbol{J}_i = 0$ lead to

$$\phi \frac{\partial c}{\partial t} + \nabla.(c\boldsymbol{\vartheta}) = 0. \qquad (5)$$

This overall balance equation can replace the balance equation of one of the components in Equation 1 such as the n_c-th component. The system of balance equations for $(n_c - 1)$ components and the overall balance equation can then be expressed in the form

$$\phi \frac{\partial c}{\partial t} + \nabla.(c\boldsymbol{\vartheta}) = 0,$$
$$\phi \frac{\partial \varsigma_i}{\partial t} + \nabla.(\varsigma_i \boldsymbol{\vartheta}) + \nabla.\boldsymbol{J}_i = 0 \quad i = 1, \dots, n_c - 1, \qquad (6)$$

where, $\varsigma_i = cz_i$ for $i = 1, \dots, n_c - 1$. In this work, the reservoir boundaries are assumed impermeable. Therefore, the convection and diffusion fluxes across the outer boundaries are zero, ie,

$$\boldsymbol{\vartheta}.\boldsymbol{n} = 0 \quad \text{on} \quad \Gamma,$$
$$\boldsymbol{J}_i.\boldsymbol{n} = 0 \quad i = 1, \dots, n_c - 1 \text{ on} \quad \Gamma, \qquad (7)$$

where Γ denotes the outer boundary of Ω and $\boldsymbol{n}$ is the unit outward normal to Γ.

3 | NUMERICAL APPROXIMATION

The DG and MFE methods are used to solve the coupled system of Equations 2,3,6, and 7. In previous works,[19-21,45] a detailed description of this method in approximating the pure convection flow equations ($\boldsymbol{J}_i = 0$) in homogeneous and fractured media was provided. In this work, we briefly review the numerical formulation and extend the method to approximate the diffusion fluxes. We focus on the calculation of diffusion and convection fluxes. The governing equations are solved by the implicit method for pressure and explicit method for composition (IMPEC).

The domain Ω is discretized into an unstructured triangular or rectangle mesh with no restrictions on the geometrical shape of the cells. We consider the following notations:

K : mesh cell,
E : edge of cell K,
N_e : number of edges for each cell ($N_e = 3$ or 4),
N_K : number of cells in a mesh,
N_E : number of edges in a mesh.

The construction of the numerical process is organized as follows:

1. discretization of Darcy's law by the MFE method,
2. discretization of the flow equations by the DG method,
3. system construction.

3.1 | Discretization of Darcy's law

In the MFE method, both the pressure and its gradient are approximated simultaneously; the velocity field is approximated in the so-called Raviart-Thomas space of the lowest order (RT_0). With this method, the velocity over each cell can be expressed in terms of the fluxes across the edges. Additional details of the MFE method was presented our other works.[19-21]

Using the Raviart-Thomas approximation space, the vectors $\boldsymbol{\vartheta}$ and $\boldsymbol{g}$ can be expressed as

$$\boldsymbol{\vartheta} = \sum_{E \in \partial K} q_{K,E} w_{K,E} \quad \text{and} \quad \boldsymbol{g} = \sum_{E \in \partial K} q^g_{K,E} w_{K,E}, \tag{8}$$

where $w_{K,E}$ is the RT_0 basis function, $q_{K,E}$ is the total volumetric convection flux across edge E, and $q^g_{K,E}$ is the flux from the gravitational force. The basis function $w_{K,E}$ has the following properties:

$$\nabla . w_E = \frac{1}{|K|}, \tag{9}$$

$$w_E . \boldsymbol{n}_{E'} = \begin{cases} 1/|E|, & \text{if } E = E' \\ 0, & \text{if } E \neq E'. \end{cases} \tag{10}$$

Therefore, the velocity field over each cell is determined by the normal fluxes across the cell edges (see Equation 8). Multiplying Equation 2 by the test function $w_{K,E}$ and integrating by parts, the total flux $q_{K,E}$ through edge E is given as a function of the cell average pressure p_K and the edge average pressures $tp_{K,E}$ in cell K, ie,

$$q_{K,E} = \alpha_{K,E} p_K - \sum_{E' \in \partial K} \left(B_K^{-1}\right)_{E,E'} tp_{K,E'} - \beta_{K,E} E \in \partial K, \tag{11}$$

where

$$(B_K)_{E,E'} = \int_K w_{K,E} K_K^{-1} w_{K,E'}$$

$$(\tilde{B}_K)_{E,E'} = \int_K w_{K,E} w_{K,E'}$$

$$\alpha_{K,E} = \sum_{E' \in \partial K} \left(B_K^{-1}\right)_{E,E'}$$

$$\beta_{K,E} = -\rho_K \sum_{E' \in \partial K} \left(B_K^{-1} \tilde{B}_K\right)_{E,E'} q^g_{K,E'}.$$

Note that the coefficients $(B_K)_{E,E'}$, $(\tilde{B}_K)_{E,E'}$, and $\alpha_{K,E}$ depend on the geometrical shape of the elements and the local mobility coefficient. By imposing the flux continuity across the cell interfaces, $(q_{K,E} = q_{K',E}; \quad E = K \cap K')$, one can eliminate the flux unknowns $q_{K,E}$ from Equation 11. As a result, the following linear system with primary unknowns, ie, the cell average pressures in P and the edge average pressures in T_P, becomes

$$R^T P - M T_P - I = 0, \tag{12}$$

where

$$R = \left[R_{K,E}\right]_{N_K, N_E} \quad ; \quad R_{K,E} = \alpha_{K,E} \quad E \in \partial K,$$

$$M = \left[M_{E,E'}\right]_{N_E, N_E} \quad ; \quad M_{E,E'} = \sum_{E,E' \supset \partial K} \left(B_K^{-1}\right)_{E,E'},$$

$$I = [I_E]_{N_E} \quad ; \quad I_E = \begin{cases} \beta_{K,E} & E \in \Gamma \\ \beta_{K,E} + \beta_{K',E} & E = K \cap K'. \end{cases}$$

3.2 | Discretization of the flow equations

The DG method is used to discretize the flow equations, ie, Equation 6. For simplicity, we apply the DG method to the flow equation of component i ($i < n_c$). Over each cell K, the unknown ς is approximated in a piecewise discontinuous linear (on triangles) or bilinear (on quadrilaterals) finite element space so that

$$\varsigma_{K,i} = \sum_{j=1}^{N_e} \varsigma_{K,i}^j \varphi_{K,j}, \tag{13}$$

where $\varphi_{K,j}$ is the finite element shape functions. Multiplying the flow equation 6 by the test functions $\varphi_{K,l}$ and integrating by parts produces volume and surface integrals that have to be evaluated over each cell, ie,

$$\int_K \phi \frac{\partial \varsigma_{K,i}}{\partial t} \varphi_{K,l} - \int_K \varsigma_{K,i} \boldsymbol{\vartheta}. \nabla \varphi_{K,l} + \int_{\partial K} \varsigma_{K,i} \varphi_{K,l} \boldsymbol{\vartheta}.\boldsymbol{n} - \int_K \boldsymbol{J}_i . \nabla \varphi_{K,l} + \int_{\partial K} \varphi_{K,l} \boldsymbol{J}_i.\boldsymbol{n} = 0 \quad l = 1, \ldots, N_e. \tag{14}$$

The volume integrals in Equation 14 can be readily calculated. However, due to the discontinuity of the functions at finite element boundaries, the surface integrals describing the convection and diffusion fluxes have to be properly defined. The convection and diffusion fluxes are modeled differently, as described in the following sections.

3.2.1 | Convection fluxes

An accurate convection flux is essential for properly simulating the flow equations. For this reason, we choose to approximate the flow velocity by the MFE method. Using Equation 10, the convection flux in Equation 14 simplifies to

$$
\int_{\partial K} \varsigma_{K,i}\varphi_{K,l}\boldsymbol{\vartheta}.\boldsymbol{n} = \int_{\partial K} \varsigma_{K,i}\varphi_{K,l}\left(\sum_E q_{K,E}w_{K,E}\right).\boldsymbol{n}
$$

$$
= \sum_E q_{K,E}\int_E \varsigma_{K,i}\varphi_{K,j}w_{K,E}.\boldsymbol{n}_E = \sum_E \frac{q_{K,E}}{|E|}\int_E \varsigma_{K,i}\varphi_{K,j}. \tag{15}
$$

Since the concentration variable $\varsigma_{i,K}|_E$ at the cell boundary E is allowed to be discontinuous, this term is treated by an upwind scheme, ie,

$$
\varsigma_{i,K}|_E = \begin{cases} \varsigma_{i,K}^{\text{in}}, & \text{if } q_{K,E} > 0 \\ \varsigma_{i,K}^{\text{out}}, & \text{otherwise.} \end{cases} \tag{16}
$$

The 2-point unwinding technique is sufficient to keep the DG method stable when using piecewise constant approximations. However, for higher-order approximations, an efficient slope limiter is needed.[19,46]

The volumetric flux is computed from Equation 11 as a function of the cell average pressure and the average edge pressures. For structured grids, one can prove that the flux in the MFE with some approximations of the integrals is equivalent to the flux in the FD method.[22] However, for unstructured grids, the FD method looses accuracy. For gas injection problems, we showed in our other work[19] that using the 2-point FD technique to approximate fluxes as an alternative to the MFE method can be useful in grids of good quality (such as equilateral triangles). This study shows that, to model natural convection, the FD approximation leads to inaccuracies in the velocity field even when using grids with good quality. The main reason is that, with natural convection, the velocity field is often very small (in the order of 10^{-10} m/s). Therefore, to get meaningful simulations, the numerical errors generated by the method have to be smaller in magnitude than the velocity values, which were found to be a challenge for the FD method. A numerical example (Example 1) is introduced to clarify this statement.

3.2.2 | Diffusion fluxes

Using the expression for $\boldsymbol{J}_i$, the total diffusion flux in Equation 4 is expanded to

$$
\int_K \varphi_{K,l}\boldsymbol{J}_i.\boldsymbol{n} = -\sum_{j=1}^{n_c-1}\int_{\partial K} \varphi_{K,l}\tilde{D}_{ij}^M\nabla z_j.\boldsymbol{n} - \int_{\partial K} \varphi_{K,l}\tilde{D}_i^p\nabla p.\boldsymbol{n} - \int_{\partial K} \varphi_{K,l}\tilde{D}_i^T\nabla T.\boldsymbol{n}, \tag{17}
$$

where $\tilde{D}_{ij}^M = cD_{ij}^M, \tilde{D}_i^p = cD_i^p,$ and $\tilde{D}_i^T = cD_i^T$. The thermal, pressure, and Fickian fluxes are approximated differently as described in the following.

Thermal diffusion flux

The thermal diffusion is expressed using the integral

$$
f_i^T = -\int_{\partial K} \varphi_{K,l}\tilde{D}_i^T\nabla T.\boldsymbol{n}. \tag{18}
$$

We assume that the temperature T is known in the domain. Usually, T is considered to be a linear function of the spatial coordinates. The coefficient $\tilde{D}_i^T$ at the cell interface E is determined according to the upstream direction of the driving force, ie,

$$
\tilde{D}_i^T|_E = \begin{cases} \tilde{D}_i^{T,\text{in}}, & \text{if } \nabla T.\boldsymbol{n}_E > 0 \\ \tilde{D}_i^{T,\text{out}}, & \text{otherwise.} \end{cases}
$$

Pressure diffusion flux

The pressure diffusion flux is expressed by

$$f_i^p = -\int_{\partial K} \varphi_{K,l} \tilde{D}_i^p \nabla p . \boldsymbol{n} . \tag{19}$$

The MFE approximation allows expressing the pressure gradient vector by flux $q_{K,E}^p$ across the edge so that

$$-\nabla p = \sum_{E \subset \partial K} q_{K,E}^p w_{K,E} . \tag{20}$$

Similar to Equation 11, $q_{K,E}^p$ is written as a function of the cell average pressure and the pressure traces

$$q_{K,E}^p = \tilde{\alpha}_{K,E} p_K - \sum_{E' \in \partial K} \left(\tilde{B}_K^{-1} \right)_{E,E'} t p_{K,E'} \qquad E \in \partial K, \tag{21}$$

where $(\tilde{B}_K)_{E,E'} = \int_K w_{K,E} w_{K,E'}$ and $\tilde{\alpha}_{K,E} = \sum_{E' \in \partial K} (\tilde{B}_K^{-1})_{E,E'}$. Using Equations 20 and 10, we get

$$f_i^p = \sum_E \frac{q_{K,E}^p}{|E|} \int_E \tilde{D}_i^p \varphi_{K,j} . \tag{22}$$

This expression is similar to the convection flux given in Equation 15. The coefficient $\tilde{D}_i^p$ is evaluated as

$$\tilde{D}_i^p \Big|_E = \begin{cases} \tilde{D}_i^{p,\text{in}}, & \text{if } q_{K,E}^p > 0 \\ \tilde{D}_i^{p,\text{out}}, & \text{otherwise.} \end{cases} \tag{23}$$

We note that the pressure unknown in Equation 22 is modeled implicitly.

Molecular diffusion flux

We express the molecular diffusion flux of component i as follows:

$$f_i^M = -\int_{\partial K} \varphi_{K,l} \tilde{D}_{ii}^M \nabla z_i . \boldsymbol{n} . \tag{24}$$

Other fluxes for cross-diffusion are treated in a similar way. We present 2 distinct approaches to approximate Equation 24 by both the MFE and LDG methods. Each approach has advantages and drawbacks as explained in the following.

Diffusion flux by the MFE method

We denote by $z_K = \frac{1}{|K|} \int_K z_i$ and $tz_{K,E} = \frac{1}{|E|} \int_E z_i$ the cell and edge averages of z_i, respectively. Note that the subscript i is dropped to simplify the notation. We also introduce an auxiliary variable ϑ^z as

$$\vartheta^z = -\tilde{D}_{ii}^M \nabla z_i . \tag{25}$$

Using the Raviart-Thomas basis function, ϑ^z can be expressed in terms of the flux unknowns

$$\vartheta^z = \sum_E q_{K,E}^z w_{K,E} . \tag{26}$$

Multiplying Equation 25 by function $w_{K,E}$ and integrating by parts yields

$$q_{K,E}^z = \alpha_{K,E}^z z_K - \sum_{E' \in \partial K} \left(B_K^{-1} \right)_{E,E'}^z t z_{K,E'} \qquad E \in \partial K, \tag{27}$$

where $(B_K)_{E,E'}^z = \int_K \tilde{D}_{ii}^M w_{K,E} w_{K,E'}$ and $\tilde{\alpha}_{K,E}^z = \sum_{E' \in \partial K} (B_K^{-1})_{E,E'}^z$.

Following the same technique used to discretize Darcy's law, we impose the continuity of the fluxes $q_{K,E}^z$ to construct the following linear system:

$$\hat{M} T_Z = \hat{R}^T Z, \tag{28}$$

where

$$\hat{R} = [\hat{R}_{K,E}]_{N_K}, N_E, \quad \hat{R}_{K,E} = \alpha^z_{K,E} \quad E \in \partial K$$

$$\hat{M} = [\hat{M}_{E,E'}]_{N_E,N_E}, \quad \hat{M}_{E,E'} = \sum_{E,E' \supset \partial K} \left(B_K^{-1}\right)^z_{E,E'}$$

$$Z = [z_K]_{N_K}, \text{ and } T_Z = [tz_E]_{N_E}.$$

The procedure is then complete to compute the fluxes. For a given compositional distribution Z, T_Z is calculated by solving the linear system in Equation 28. The flux $q^z_{K,E}$ can then be computed locally from Equation 27. Although matrix $\hat{M}$ is symmetric and a positive definite, solving Equation 28 for each time step and for each component can potentially be expensive. However, by using the upstream values of the coefficients at the cell boundaries, $\hat{M}$ becomes dependent on the finite element geometries only. Therefore, one way to accelerate the calculation is to store the Cholesky decomposition of $\hat{M}$ (once at the start of the simulation); the calculation of the fluxes for each component is then reduced to the cost of solving 2 triangular linear systems. In the following section, we present an alternative approach to evaluate Equation 24 by using the LDG method.

Diffusion fluxes by the LDG method

The LDG method possesses features that are similar to the MFE method. One of them is that the primary unknown and its gradient are approximated simultaneously. The LDG method conserves mass locally and is flexible for high-order approximations. The main difference between the LDG and MFE methods is that, in the LDG method, the fluxes can be calculated locally, whereas different fluxes approximated by the MFE are computed through a global linear system. For each cell K, we introduce the auxiliary variable v_K so that

$$v_K = -\tilde{D}_{ii}^M \nabla z_{i,K}. \tag{29}$$

Letting $v_K = (q_{x,K}, q_{y,K})^T$ and substituting into Equation 24, we obtain

$$f_i^M = \int_{\partial K} \varphi_{K,l} v_K . \boldsymbol{n}_K$$

$$= \int_{\partial K} \varphi_{K,l}(q_{x,K} n_{x,K} + q_{y,K} n_{y,K}), \tag{30}$$

where $\boldsymbol{n}_K = (n_{x,K}, n_{y,K})$ is the outward unit vector to the boundary E. Due to the discontinuity of v_K at the interface, Equation 30 is replaced by

$$f_i^M = \int_{\partial K} \varphi_{K,l} \hat{v} . \boldsymbol{n}_K$$

$$= \int_{\partial K} \varphi_{K,l}(\hat{q}_x n_{x,K} + \hat{q}_y n_{y,K}). \tag{31}$$

Multiplying Equation 30 by a test function φ and integrating by parts, we obtain

$$\int_K \frac{1}{\tilde{D}_{ii}^M} q_{x,K} \varphi = \int_K z_{i,K} \frac{\partial \varphi}{\partial x} - \int_{\partial K} \varphi \hat{z}_i n_{x,K},$$

$$\int_K \frac{1}{\tilde{D}_{ii}^M} q_{y,K} \varphi = \int_K z_{i,K} \frac{\partial \varphi}{\partial y} - \int_{\partial K} \varphi \hat{z}_i n_{y,K}. \tag{32}$$

The terms $\hat{v}$ and $\hat{z}_i$ (with "hats") are the numerical fluxes at the boundary that link the 2 elements. A crucial aspect of the LDG method for stability is the proper choice of these numerical fluxes. Different choices are possible to define the numerical fluxes; here, we adopt the formulation given in the work of Hoteit et al.[46] At each edge E separating 2 cells K and K' ($E = K \cap K'$), the unknowns z_i and v calculated within K and K' are discontinuous. The numerical fluxes are defined in terms of the jumps and the averages at the cell boundaries. The jump and average are defined separately for scalars and vectors. For a vector, the jump and average at E are, respectively, defined as follows:

$$\{z_i\} = \frac{1}{2}(z_{i,K} + z_{i,K'})$$

$$[z_{i,K}] = z_{i,K} \boldsymbol{n}_K + z_{i,K'} \boldsymbol{n}_{K'}. \tag{33}$$

For a scalar, the jump and average are

$$\{v\} = \frac{1}{2}(v_K + v_{K'})$$
$$[v] = v_K \cdot \boldsymbol{n}_K + v_K \cdot \boldsymbol{n}_{K'}.$$

(34)

Note that the jump of a scalar is a vector and that the jump of a vector is a scalar. The numerical fluxes appearing in Equations 31 and 32 are then

$$\hat{z}_i = \{z_i\} + \gamma \cdot [z_i], \quad \hat{v} = \{v\} - \beta \cdot [v].$$

(35)

Here, we set $\gamma = (1, 1)$ and $\beta = 1$ to achieve an optimal convergence.[47] These terms control the introduced numerical dispersion necessary to keep the method numerically stable. By neglecting these terms and using structured grids, the method reduces to the conventional cell-centered FD method.[37] Using Equations 32 and 35, the numerical fluxes can be computed by solving a local linear system. However, due to the discontinuity of velocity at the interelements, the LDG method loses accuracy as compared with the MFE method. A numerical test in Example 2 is devoted to compare the MFE and LDG methods.

3.3 | System construction

The Newton-Raphson method is used to linearize the coupled systems from Equations 3, 12, and 15. An IMPEC scheme is implemented, in which the pressure unknowns are modeled implicitly and the composition unknowns are modeled explicitly in time. The diffusion fluxes, except for the pressure diffusion, are explicitly in time, and therefore, they are treated as a sink/source terms. A full description of the algorithm is provided in other works.[19-21,45]

4 | NUMERICAL RESULTS

In this section, we present the results of calculations from the algorithm described above for various examples covering homogeneous, heterogeneous, and fractured media. Two-, three- and ten-component fluid mixtures are used in the examples. One of the examples is a tilted reservoir.

Example 1. In this example, we investigate the accuracies of the velocity fields approximated by the MFE and the conventional 2-point FV method. We consider a rectangular cross-sectional domain saturated with a hydrocarbon mixture of C_1/nC_4 (see Table 1). The permeability in the domain is 1 mD, except in one zone where its value is 10^{-3} mD (see Figure 1). The domain is discretized into an unstructured triangular mesh. Two different cases are considered. In the first case, no fluid injection was considered and the fluid flow is solely from natural convection. Figure 1A shows the velocity field from the 2-point FV approximation. Although, the mesh quality is good as all triangular cells are almost equilateral, inaccuracy in the velocity field is clearly observed. In Figure 1B, the velocity field approximated by the MFE method has no apparent inaccuracy. The poor accuracy of the FV method is related to the magnitude of the velocity field, which is apparently within the order of magnitude of the numerical error introduced by the method (approximately 5×10^{-10} m/s). To examine this hypothesis, we introduce a second case where the velocity is increased in the domain by injecting C_1 in the left lower corner and producing C_1/nC_4 from the diagonally opposite corner. The injection rate is 10^{-2} m³/day, and the velocity is in the order of 10^{-7} m/s. In this case, the FV and MFE methods provide nearly the same results. Figure 2 shows the velocity fields calculated by both methods. We conclude that a method with a higher order of approximation such as the MFE method is required to accurately approximate the velocity field in natural convection.

TABLE 1 Data for Examples 1-3 and 5

|	
Pressure at domain center	111.4 bar
Temperature at domain center	339.15 K
Horizontal temperature gradient	3.34 K/1000 m
Vertical temperature gradient	6.67 K/100 m
Porosity	25%
Composition at domain center	20%C_1, 80%nC_4
Permeability	0-1000 mD
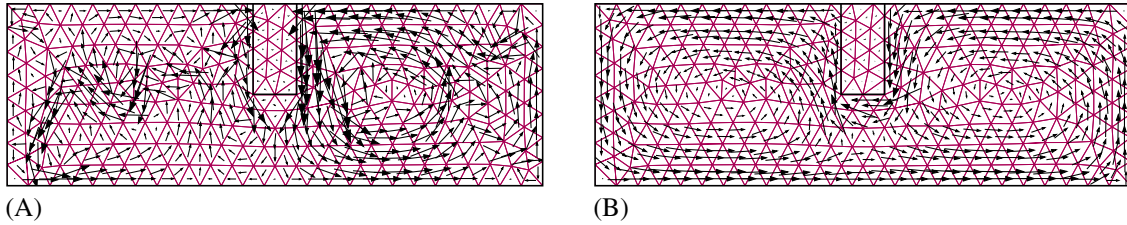
FIGURE 1 Velocity field by the finite-volume (FV) and mixed finite element (MFE) methods; natural convection; max velocity $\approx 5 \times 10^{-10}$ m/s; Example 1, Case 1. A, Two-point FV; B, MFE [Colour figure can be viewed at wileyonlinelibrary.com]
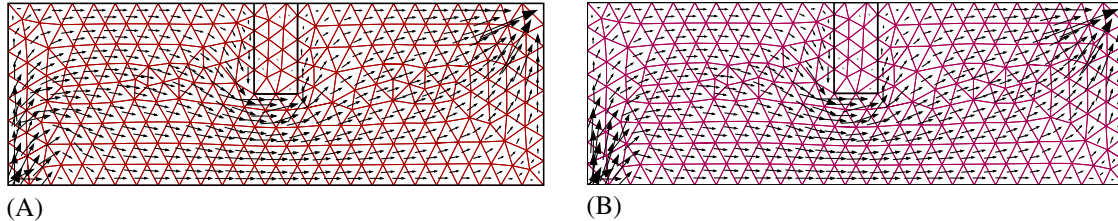

FIGURE 2 Velocity field by the finite-volume (FV) and mixed finite element (MFE) methods; gas injection at the lower left corner, fluid production through the opposite corner; max velocity $\approx 10^{-7}$ m/s; injection rate $= 10^{-2}$ m³/day; Example 1, Case 2. A, Two-point FV; B, MFE [Colour figure can be viewed at wileyonlinelibrary.com]

Example 2. In this example, we investigate the accuracy of MFE and LDG methods in calculating the Fickian diffusion flux. The main advantage of the LDG method is in its flexibility to compute the fluxes locally with a high-order approximation. For computational efficiency, we use a first-order approximation. In the DG method, local linear systems are solved to compute the fluxes. In the MFE method, however, a global linear system is solved to compute the fluxes. The LDG method is more efficient, but it is generally less accurate than the MFE method. The superiority of the MFE method was reported in the work of Fagherazzi et al.[47]

We consider a vertical domain of dimensions ($L_z = 100$ m, $L_x = \Delta x$ m) saturated with a binary mixture C_1/nC_4 (Table 1). The domain is discretized into 1 column of right-angled triangles (see Figure 3A). We fix the number of cells in the mesh (ie, fixed Δz) and vary the column base, Δx. The accuracies of the LDG and MFE methods are investigated when the ratio $\kappa = \Delta x/\Delta z$ is varied. When κ increases, the triangles tend to flatten. In Figure 3B, C_1 composition versus height calculated from the LDG and MFE methods is presented for different values of κ. The change in C_1 composition profiles as a function of κ in the LDG solution is unphysical. This variation is a result of mesh dependency. On the other hand, the MFE method shows almost no mesh dependency (Figure 3B). The mesh
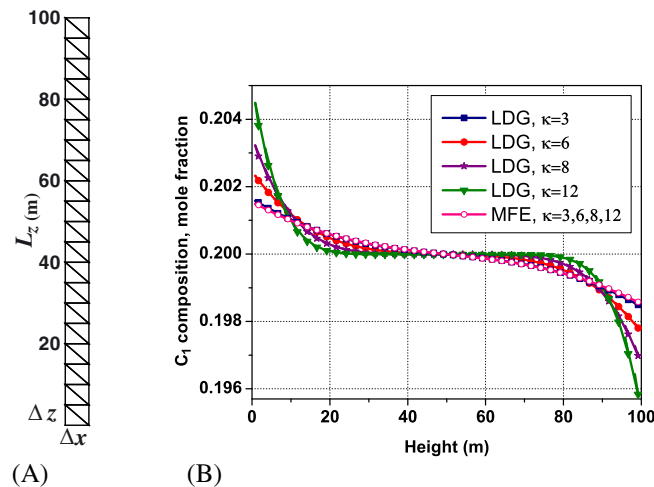

FIGURE 3 Mesh consisting of 1 column of right-angled triangles and distribution of C_1 composition computed by the local discontinuous Galerkin (LDG) and mixed finite element (MFE) methods as a function of the ratio κ; Example 2. A, Mesh; B, C_1 mole fraction versus height [Colour figure can be viewed at wileyonlinelibrary.com]
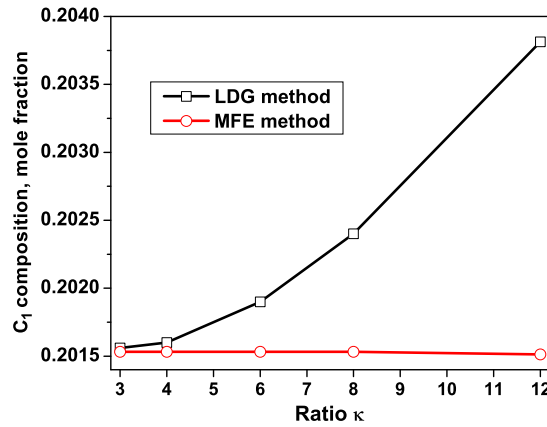
FIGURE 4 Variation of C_1 composition as a function of κ at a fixed point (at height = 0) in the domain by using the local discontinuous Galerkin (LDG) and mixed finite element (MFE) methods; Example 2 [Colour figure can be viewed at wileyonlinelibrary.com]

dependency can be further examined by showing C_1 composition at a fixed point in the domain for different values of κ. Figure 4 demonstrates that there is very little change in the MFE solution compared with the LDG solution. The example illustrates the superiority of the MFE method in approximating the diffusion flux in distorted grids. For good quality grids, the LDG method is preferred because of its superior efficiency. In this example, the LDG method was 40% to 50% faster than the MFE method.

Example 3. In this example, we investigate the permeability effect on the compositional variation of a binary mixture of methane and normal butane in a vertical cross-section ($L_z = 150$ m, $L_x = 3000$ m). The input data are provided
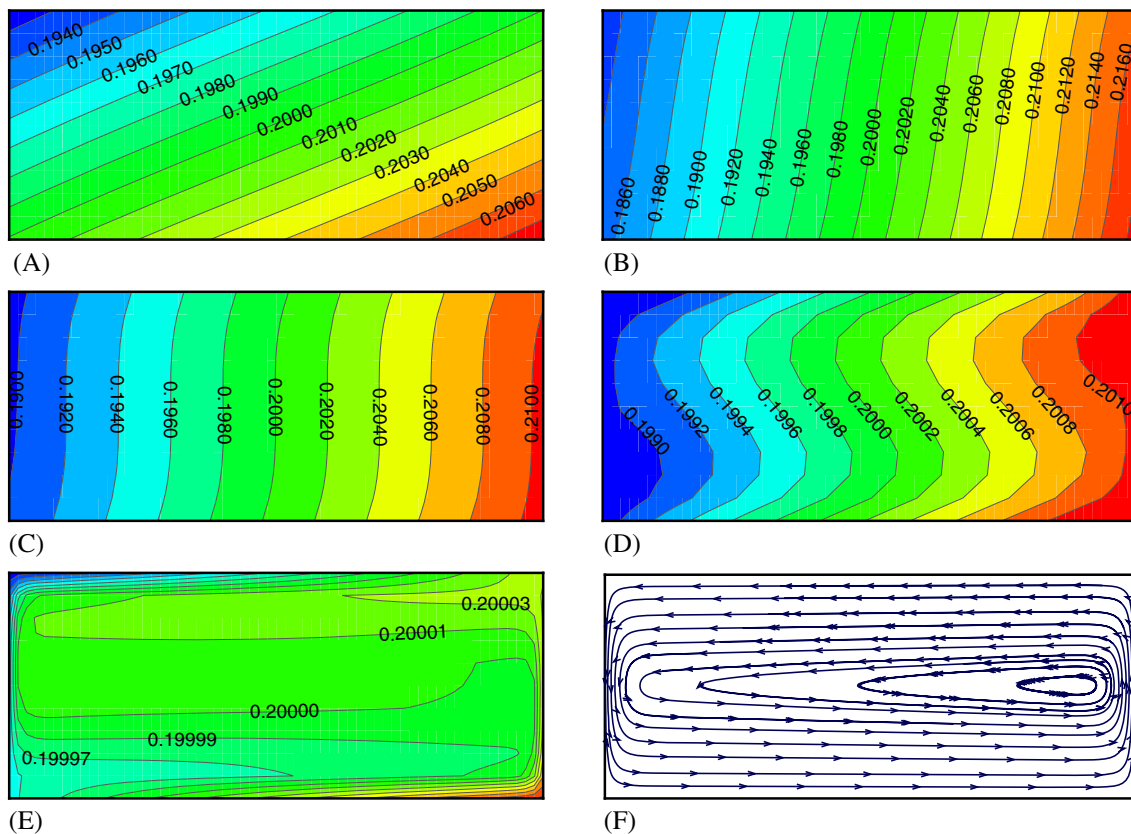
FIGURE 5 Contours of methane composition (mole fraction) for different permeabilities and velocity field corresponding to $k = 1000$ mD, binary mixture at steady state; ($L_x = 3000$ m; $L_z = 150$ m); Example 3. A, convection free; B, $k = 0.5$ mD; C, $k = 2$ mD; D, $k = 30$ mD; E, $k = 1000$ mD; F, velocity field for $k = 1000$ mD [Colour figure can be viewed at wileyonlinelibrary.com]

in Table 1. The diffusion coefficients, D_{ij}^M, D_i^p, and D_i^T (Equation 4) are calculated as a function of pressure, temperature, and composition. The methane composition contours at steady state, for different values of permeability ($k = 0, 0.5, 2, 30, 1000$ mD), are presented in Figure 5. The results are in good agreement with those presented in the work of Riley and Firoozabadi.[15] The increase of permeability k has only a minor effect on the performance of our algorithm performance. Methane tends to segregate more in the hotter region of the domain mainly due to the thermal diffusion in Figure 5A. For high permeabilities ($k > 30$ mD), the natural convection becomes more dominant, almost leading to a homogeneous distribution of the fluid (see Figure 5D and 5E). Figure 5F shows the velocity distribution in the domain for $k = 1000$ mD, for calculations performed on a structured mesh with 671 elements. The CPU time is about 250 seconds with permeability, $k = 1000$ mD. All calculations were performed on a 64-bit Intel® Xeon® PC. Although the increase of permeability reduces the time-step size because of the Courant-Friedrichs-Lewy condition, the CPU time required for the other cases ($k = 0.5, 2, 30$ mD) is of the same order. With lower permeability, more iterations on the transient equations were needed to reach the steady state.

Example 4. In this example, we compute the compositional variation in a vertical cross-section for 2 different mixtures. Our results are compared with the work of Ghorayeb and Firoozabadi.[17] In Example 4a, we use a ternary mixture of $C_1/C_2/nC_4$ and, in Example 4b, a 10-component mixture. Tables 2 and 3 provide respective relevant data. In all our simulations, the diffusion coefficients, as well as the density, are allowed to vary in space and in time, unlike in the numerical model introduced in the aforementioned work.[17] In Example 4a, the composition of the ternary mixture at the center of the reservoir is C_1 25%, C_2 25%, and C_3 50% (moles). In Figure 6, the composition contour plots for C_1 are depicted for different permeabilities ($k = 0, 1, 10, 100$ mD). We observe that C_1 is more segregated in the hot area on the right side of the domain similar to what we observe for a binary mixture. There is almost no variation in composition with an increase in permeability. In all runs, calculations are performed on a uniform grid of 671 elements. In this run and all the other runs, there is practically no change in the results from finer gridding. The

TABLE 2 Data for Example 3

|	
Pressure at domain center	70 bar
Temperature at domain center	315 K
Horizontal temperature gradient	1.8 K/1000 m
Vertical temperature gradient	3.5 K/100 m
Porosity	25%
Composition at domain center	$25\%C_1, 25\%C_2, 50\%nC_4$
Permeability	0-100 mD
Domain dimensions	$L_z = 150$ m, $L_x = 1500$ m

TABLE 3 Data for Example 4

Pressure at domain center	466 bar
Temperature at domain center	422 K
Horizontal temperature gradient	1.5 K/1000 m
Vertical temperature gradient	2.75 K/100 m
Porosity	25%
Composition at domain center	$3.229\%CO_2$
	$62.53\%C_1$
	$9.644\%C_2$
	$9.080\%C_3\text{-}nC_4$
	$3.436\%C_5\text{-}C_6$
	$5.979\%C_7\text{-}C_{10}$
	$2.450\%C_{11}\text{-}C_{14}$
	$2.085\%C_{15}\text{-}C_{20}$
	$1.288\%C_{21}\text{-}C_{29}$
	$0.556\%C_{30+}$
Permeability	0-10 mD
Domain dimensions in the $x\text{-}z$ plane	$L_z = 1500$ m, $L_x = 10\,000$ m
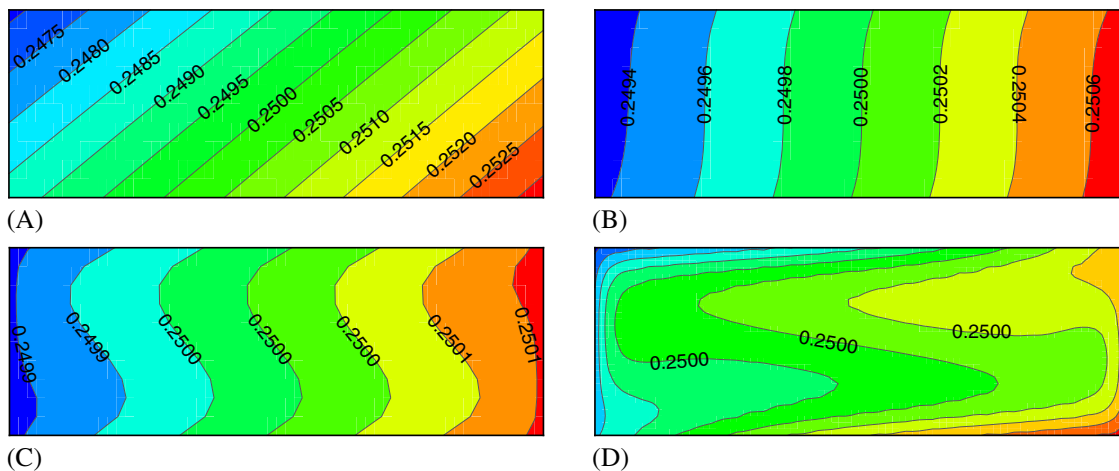
FIGURE 6 Composition contour plot for C_1, with different permeability cases, ternary mixture ($25\%C_1$, $25\%C_2$, $50\%nC_4$ at the center); ($L_x = 1500$ m; $L_z = 150$ m); Example 4a. A, convection free; B, $k = 1$ mD; C, $k = 10$ mD; D, $k = 100$ mD [Colour figure can be viewed at wileyonlinelibrary.com]

CPU time was about 400 seconds. In this run and all the other runs, there was practically no change in the results from finer gridding. Example 4b presents the results obtained with large-scale field dimensions; relevant data are listed in Table 3. Figure 7 shows composition profiles of C_1, C_5-C_6, and C_{30+} for permeabilities $k = 0$ (convection free) and $k = 10$ mD. The results are in good agreement with those in the work of Riley and Firoozabadi.[15] Methane, which has the maximum variation, segregates toward the top of the domain. However, the other components, except C_{30+}, have no significant compositional variation. Note that natural convection reduces segregation. The domain is discretized into a rectangular mesh consisting of 3321 elements. The CPU time was about 3200 seconds.
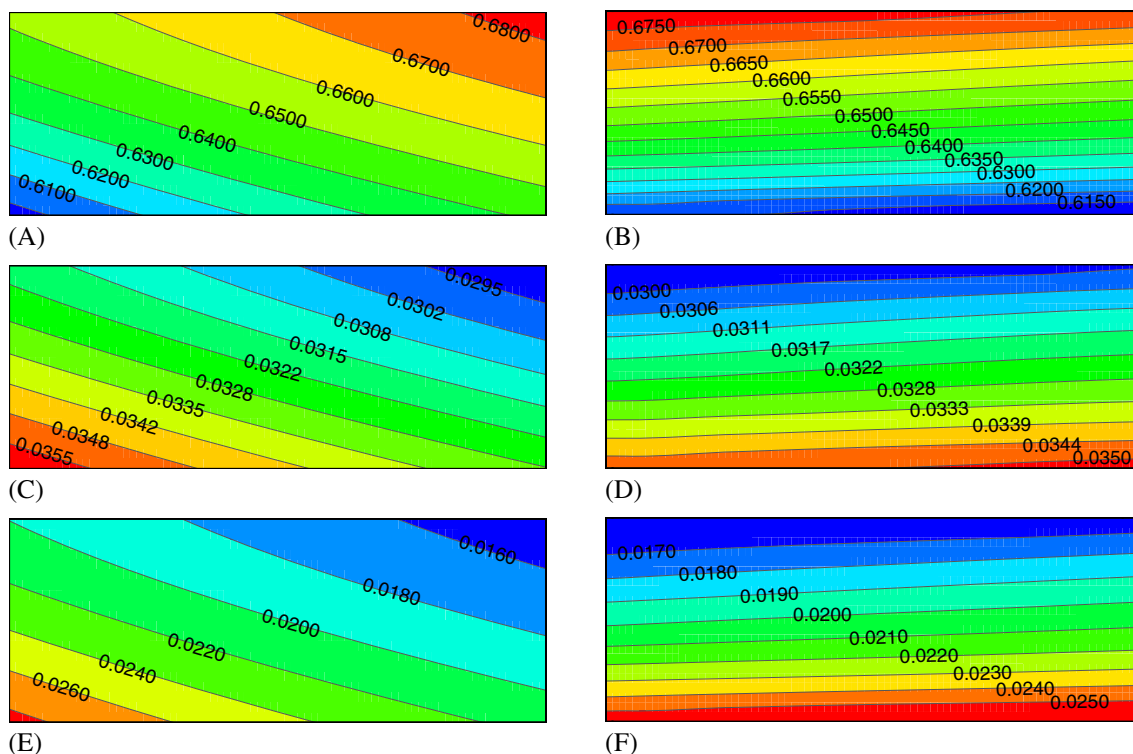

FIGURE 7 Composition contour plot for C_1, C_5-C_6, and C_{11}-C_{14}, with different permeability cases, 10-component mixture; ($L_x = 10\,000$ m; $L_z = 1500$ m); Example 4b. A, C_1, convection free; B, C_1, $k = 10$ mD; C, C_5-C_6, convection free; D, C_5-C_6, $k = 10$ mD; E, C_{11}-C_{14}, convection free; F, C_{11}-C_{14}, $k = 10$ mD [Colour figure can be viewed at wileyonlinelibrary.com]

TABLE 4 Data for Example 6

Pressure at domain center	890 bar
Temperature at domain center	360.1 K
Horizontal temperature gradient	1.8 K/1000 m
Vertical temperature gradient	3.5 K/100 m
Porosity	25%
Composition at domain center	$20\%C_1, 80\%nC_4$
Permeability	$0\text{-}10^5$ mD

Example 5. Ghorayeb and Firoozabadi[18] investigated the effect of fractures on the compositional variation of binary systems. They studied natural convection and diffusion in fractured media by using the single-porosity model in FD in which the fractured medium is treated as a heterogeneous medium with distinct matrix and fracture permeabilities. The authors reported that the discretization of the governing equations by the FD model led to ill-conditioned large systems because of (i) a sharp variation in permeability between the matrix and fractures and (ii) a small fracture aperture compared to the matrix size. Therefore, the single-porosity approach has limitations from a numerical perspective. The discrete fracture model appears to be an attractive and simpler alternative to the single-porosity model where fractures are represented by (n-1)-dimensional elements in an n-dimensional domain. We compute the compositional variation of a binary mixture C_1/nC_4 in a rectangular domain of 15 m × 30 m, where the matrix permeability is $k_m = 1$ mD, and the fracture aperture is $f_a = 1$ mm (see Table 4). Several configurations of fractures are used to study


(A) (B) (C) (D)
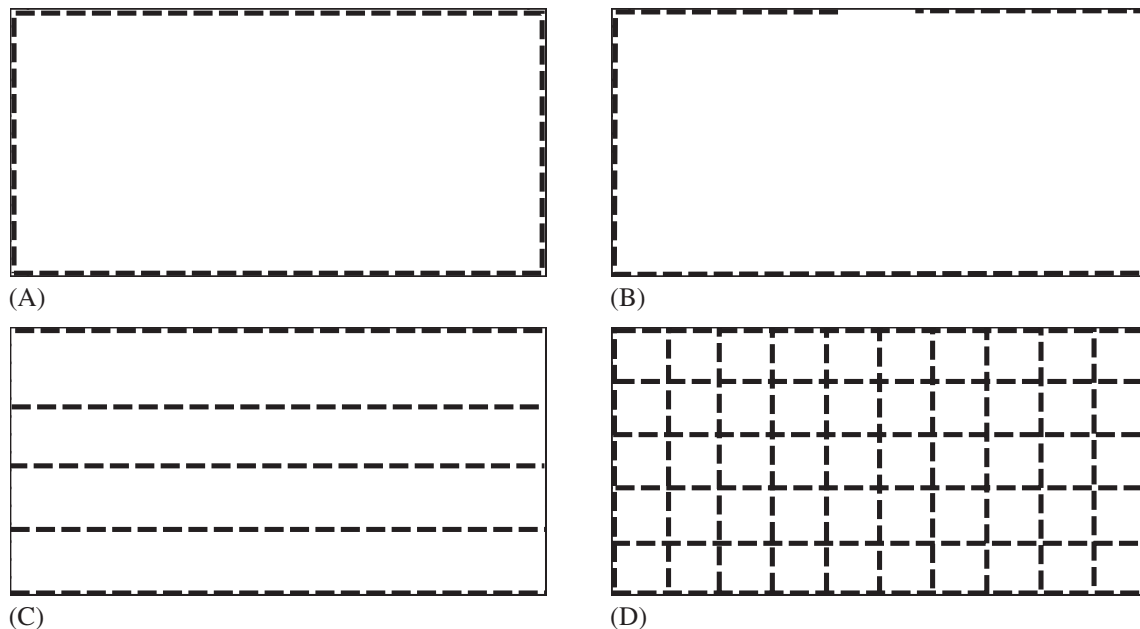
FIGURE 8 Different fracture configurations; binary mixture ($20\%C_1, 80\%nC_4$); Example 5a. A, Configuration 1; B, Configuration 2; C, Configuration 3; D, Configuration 4


(A) (B)
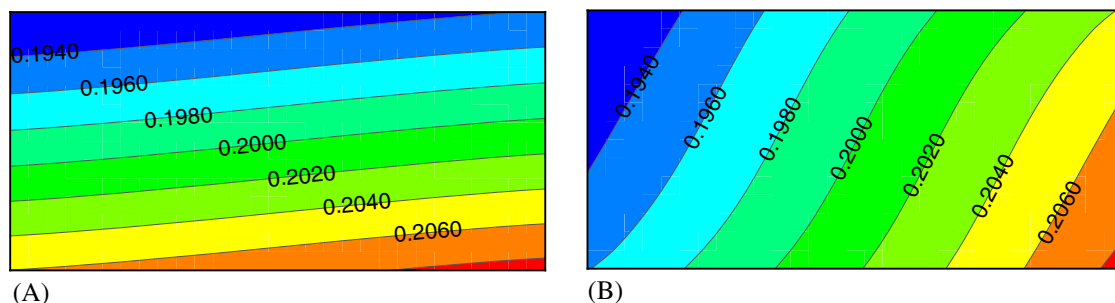
FIGURE 9 Methane mole fraction with different fracture permeabilities; ($L_x = 30$ m; $L_z = 15$ m); configuration 1, Example 5a. A, $k_f = 1$ mD; B, $k_f = 10^3$ mD [Colour figure can be viewed at wileyonlinelibrary.com]

the effect of the fracture connectivity and that of the fracture permeability, which varies from $k_f = 1$ mD (no fractures) to $k_f = 10^5$ mD (Figure 8). In configuration 1 (Figure 8A), one fracture is considered around the domain boundaries. In configurations 2 and 3, (Figure 8B and 8C) the fractures are disconnected, and configuration 4 (Figure 8D) represents a sugar cube geometry consisting of 50 matrix blocks surrounded by fractures. The methane contour lines with low fracture permeabilities are shown as references in configuration 1 (Figure 9). Figure 10 shows the methane distribution and velocity field, at steady state, for all configurations with fracture permeabilities of 10^4 and 10^5 mD. In Figure 10B, the velocity field consists mainly of one loop. The results show that the increase in fracture permeability makes the composition uniform, as expected. Disconnected fractures in configurations 2 and 3 (Figure 10D and 10F) have less effect on compositional variation. In configuration 4 (Figure 10H), composition distributions show that, unlike in configuration 1, the mole fraction contours take an "S" shape when the fracture permeability increases.
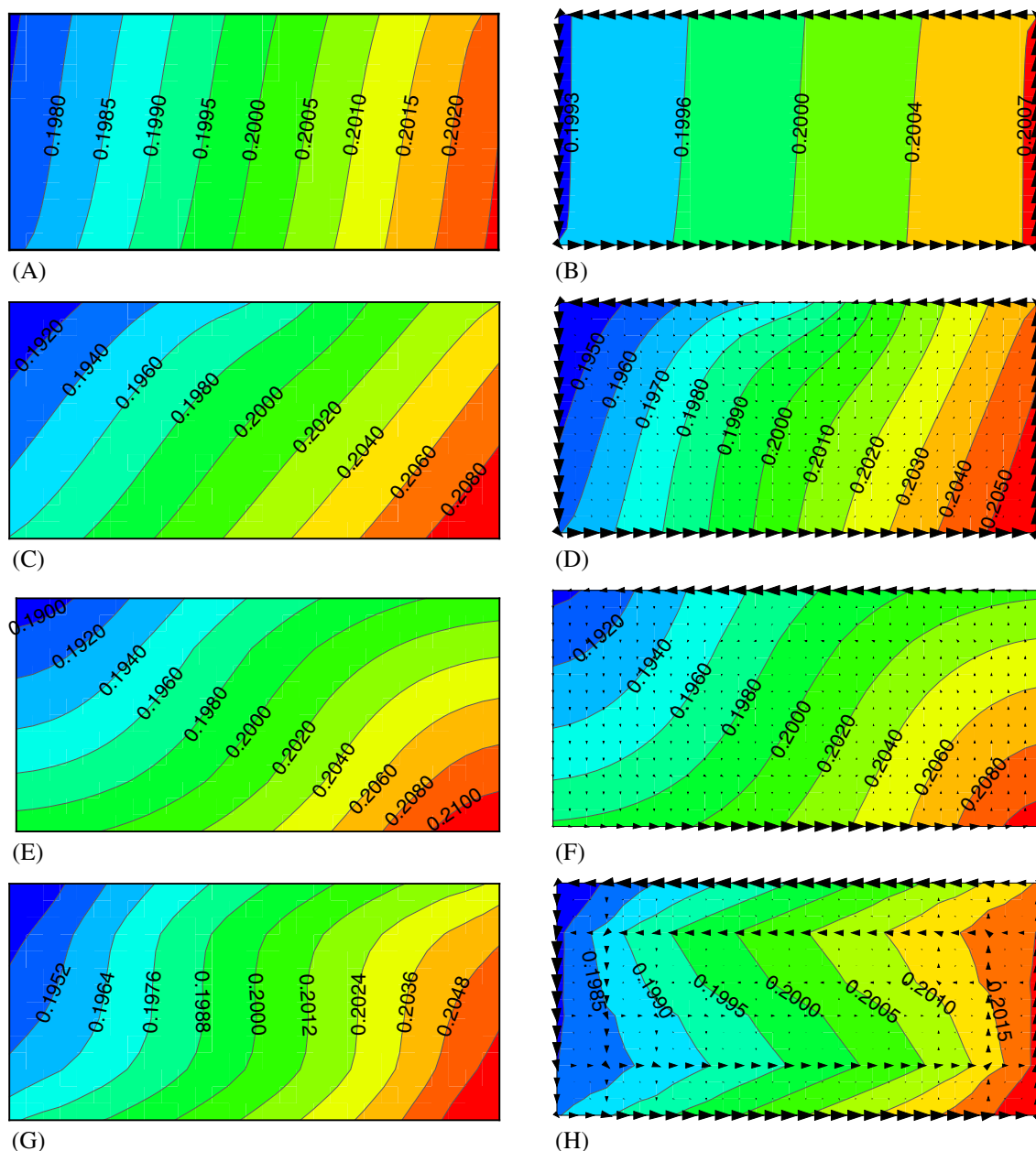
FIGURE 10 C_1 mole fraction and velocity profiles with different fracture permeabilities and configurations, ($L_x = 30$ m; $L_z = 15$ m); Example 5a. A, Configuration 1 ($k_f = 10^4$ mD); B, Configuration 1 ($k_f = 10^5$ mD); C, Configuration 2 ($k_f = 10^4$ mD); D, Configuration 2 ($k_f = 10^5$ mD); E, Configuration 3 ($k_f = 10^4$ mD); F, Configuration 3 ($k_f = 10^5$ mD); G, Configuration 4 ($k_f = 10^4$ mD); H, Configuration 4 ($k_f = 10^5$ mD) [Colour figure can be viewed at wileyonlinelibrary.com]
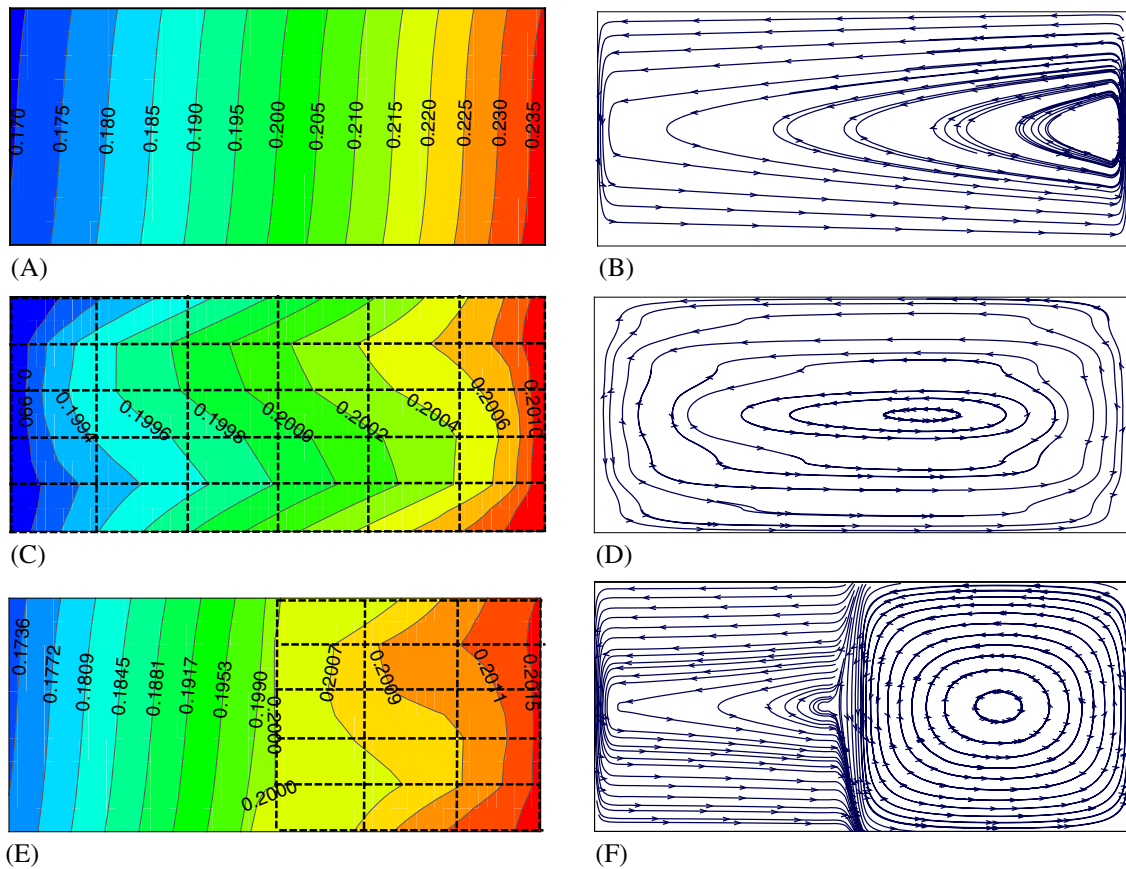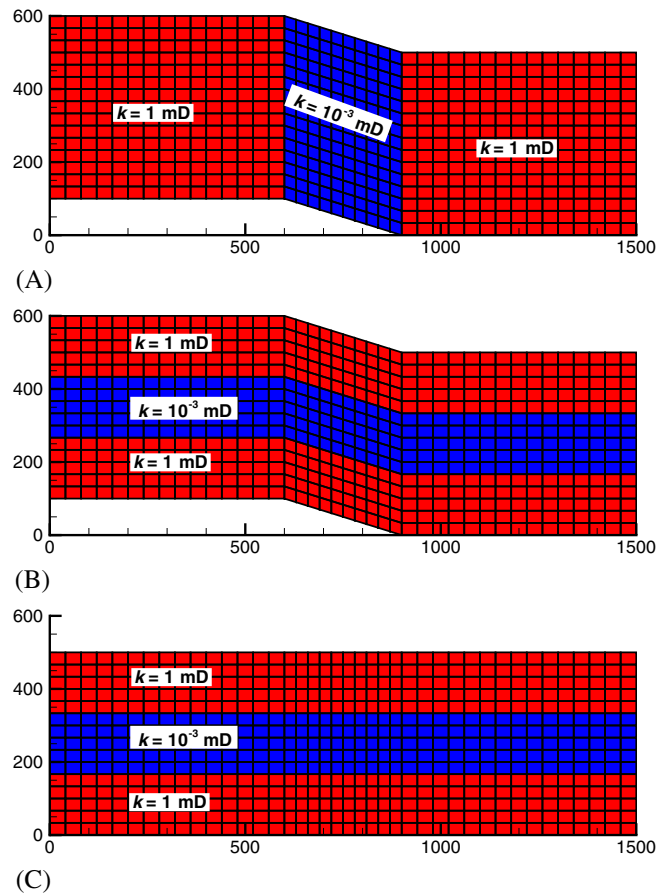
FIGURE 11 C_1 mole fraction and velocity profiles with different fracture permeabilities; ($L_x = 6000$ m; $L_z = 150$ m); Example 5b. A, Unfractured (C_1 composition); B, Unfractured (flow lines); C, Sugar cube configuration (C_1 composition); D, Sugar cube configuration (flow lines); E, Partially fractured configuration (C_1 composition); F, Partially fractured configuration (flow lines) [Colour figure can be viewed at wileyonlinelibrary.com]

Our results are in good agreement with those reported in the work of Ghorayeb and Firoozabad.[17] One advantage of our model is that the decrease in fracture thickness does not impact the computational efficiency. However, in the single-porosity model, as the contrast between the matrix and fractures increases, more refined gridding is needed. We note that the CPU time required for our calculations in configuration 4 is about 150 seconds in a uniform grid of 450 elements. The CPU times for the other cases are less than 3 minutes. The performance of our model is 2 to 3 orders of magnitude faster than the FD-based single-porosity model. The speedup is essentially due to a smaller number of grid cells needed in our model.

To show the robustness of our model, we increase the domain dimensions (150 m × 6000 m). The fracture aperture and permeability are, respectively, $f_a = 0.1$ mm and $k_f = 10^4$ mD. We consider 3 configurations: (1) homogeneous, (2) fractured with a sugar cube geometry, and (3) partially fractured domain with 2 subdomains, ie, one unfractured side and the other fractured with sugar cube configuration. The compositional variations and the flow line profiles for all configurations are shown in Figure 11. In the unfractured domain (configuration 1), there is a significant horizontal variation in the methane mole fraction at the steady state (Figure 11A and 11B). In the fractured domain (configuration 2), C_1 compositional variation is insignificant (Figure 11C and 11D). In configuration 3, C_1 composition contour lines are vertical in the homogeneous unfractured region and they display an "S" shape in the fractured zone (Figure 11E and 11F). The key conclusion is that the presence of fractures results in more effective mixing from natural convection. As a result, less compositional segregations from diffusion are observed. The CPU time for all these configurations, which are discretized uniformly into 1300 gridlocks, is about 700 seconds.

Example 6. In the last example, we investigate the compositional variation of a ternary mixture of $C_1/C_2/nC_4(C_1 35\%, C_2 35\%, nC_4 30\%)$ in a tilted domain where different configurations for heterogeneities and fractures are considered. The relevant reservoir and fluid data are listed in Table 4. In Example 6a, we consider 3
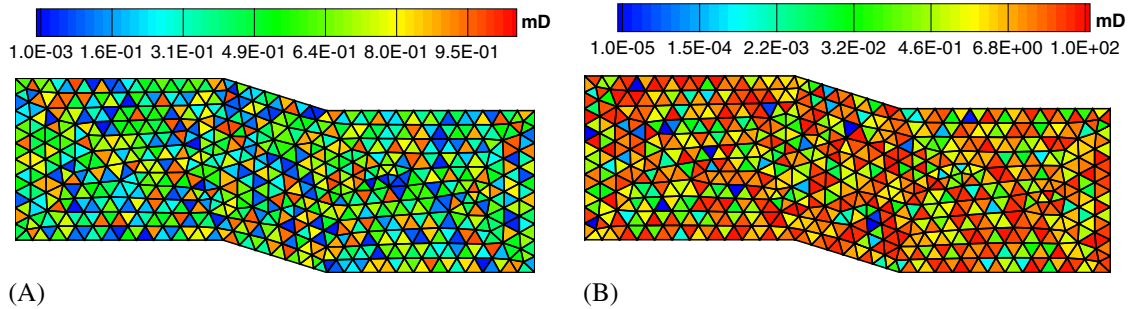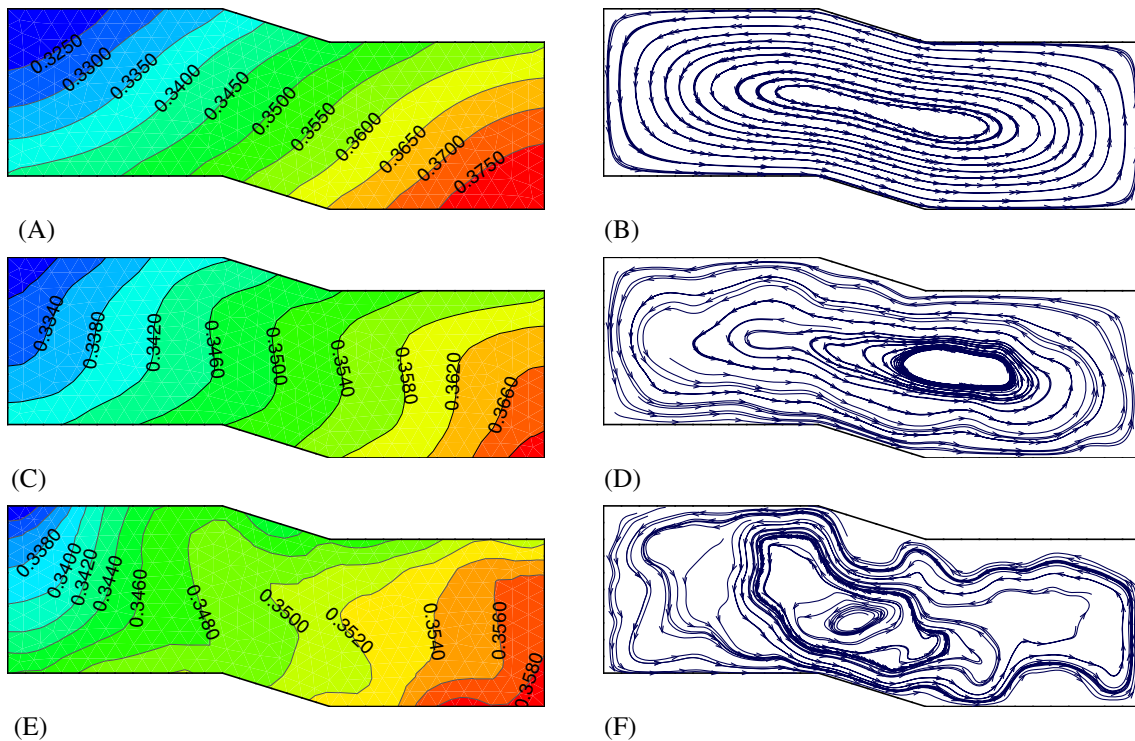
FIGURE 12 Domain with different permeable zones; (L_x = 1500 m, L_z = 600 m); Example 6a. A, Configuration 1; B, Configuration 2; C, Configuration 3 [Colour figure can be viewed at wileyonlinelibrary.com]
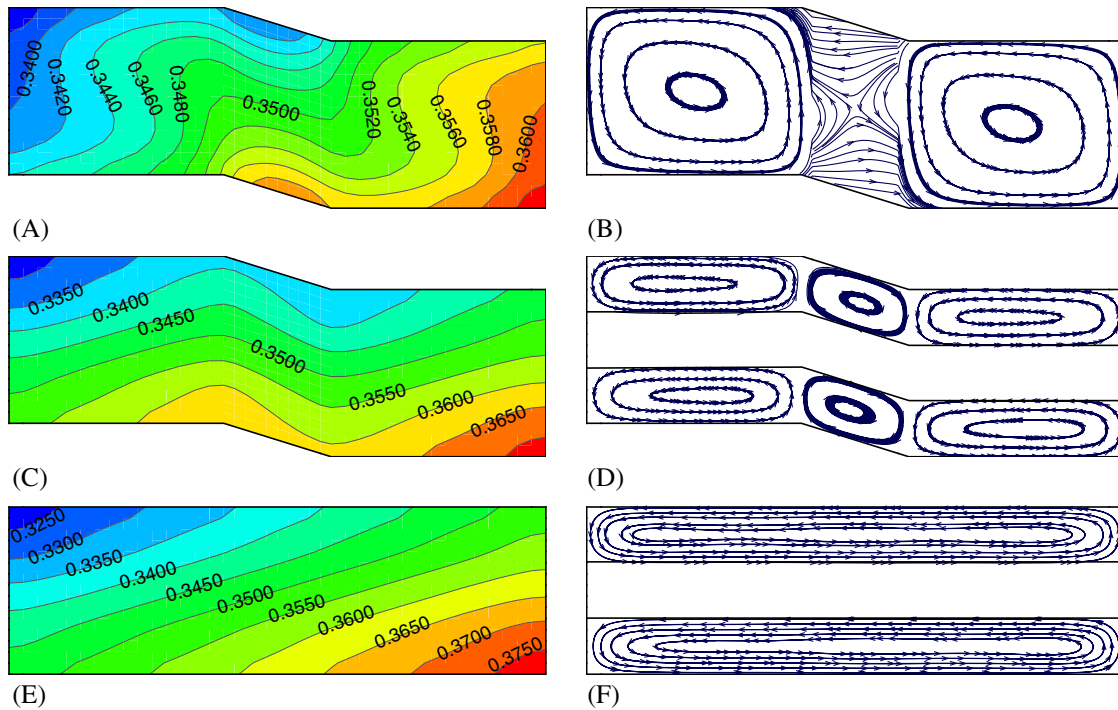
FIGURE 13 C_1 composition and velocity profiles for configurations 1 to 3, (L_x = 1500 m, L_z = 600 m); Example 6a. A, Configuration 1 (C_1 composition); B, Configuration 1 (flow lines); C, Configuration 2 (C_1 composition); D, Configuration 2 (flow lines); E, Configuration 3 (C_1 composition); F, Configuration 3 (flow lines) [Colour figure can be viewed at wileyonlinelibrary.com]
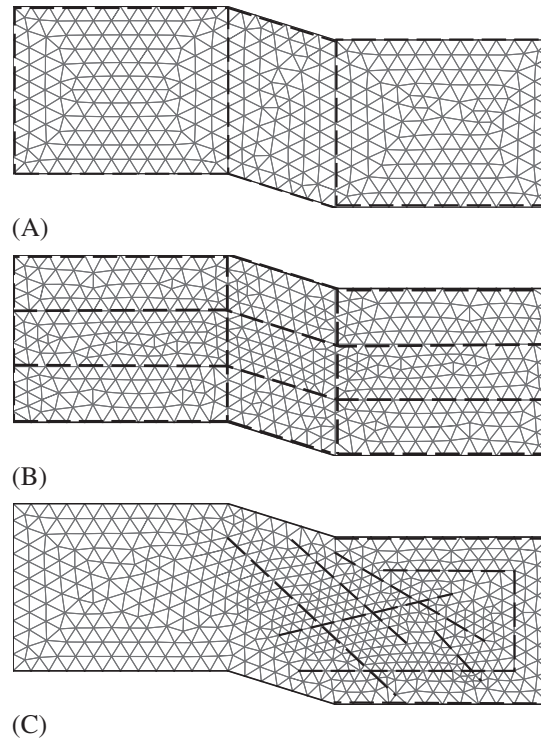
FIGURE 14 Permeability distributions for 2 configurations, ($L_x = 1500$ m, $L_z = 600$ m); Example 6b. A, Configuration 1; B, Configuration 2
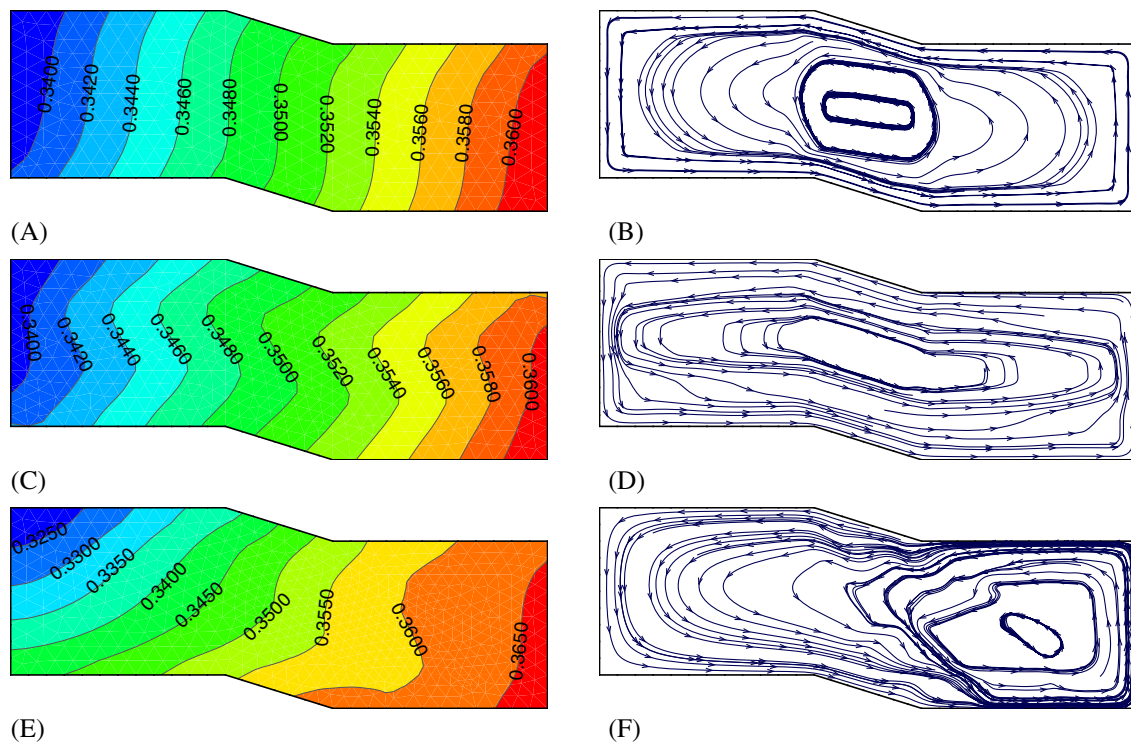

FIGURE 15 C_1 composition and velocity profiles for configurations 1 and 2, ($L_x = 1500$ m, $L_z = 600$ m); Example 6b. A, Homogeneous (C_1 composition); B, Homogeneous (flow lines); C, Configuration 1 (C_1 composition); D, Configuration 1 (flow lines); E, Configuration 2 (C_1 composition); F, Configuration 2 (flow lines) [Colour figure can be viewed at wileyonlinelibrary.com]

configurations with different permeable zones, as shown in Figure 12. The domain is discretized into an unstructured grid of quadrilaterals. The corresponding C_1 composition and velocity fields for all configurations are shown in Figure 13. Different convective loops are observed at steady state. Due to the tilted geometry in configuration 2, the contour lines have opposite slopes in the inclined zones (Figures 12A and 13B). The small velocity in the tight zone in configurations 2 and 3 preclude observation. In Example 6b, the domain in configurations 1 and 2 is discretized into a triangular mesh with heterogeneous permeabilities (Figure 14). The contrasts in permeability in configurations 1 and 2 are 3 and 7 orders of magnitude, respectively. In Figure 15, we compare the contour lines with the case where the domain is assumed homogeneous with a permeability $k = 0.1$ mD. The plots show that, in all cases, there is only one main convection cell.

In Example 6c, we consider 3 configurations of connected and disconnected fractures (Figure 16). The contour lines for C_1 composition and the velocity fields are represented in Figure 17. The results are similar to those for the rectangular domain with structured fractures. However, from a numerical perspective, this highlights the flexibility of our numerical algorithm to model unstructured domains, including those with connected and disconnected fractures.

FIGURE 16 Models with different fractured configurations; ($L_x = 1500$ m, $L_z = 600$ m); Example 6c. A, Configuration 1; B, Configuration 2; C, Configuration 3

FIGURE 17 C_1 composition and velocity profiles for configurations 1 to 3, ($L_x = 1500$ m, $L_z = 600$ m); Example 6c. A, Configuration 1 (C_1 composition); B, Configuration 1 (flow lines); C, Configuration 2 (C_1 composition); D, Configuration 2 (flow lines); E, Configuration 3 (C_1 composition); F, Configuration 3 (flow lines) [Colour figure can be viewed at wileyonlinelibrary.com]

5 | CONCLUSIONS

An efficient and robust numerical approach using the DG and MFE methods has been presented for computing compositional variation of multicomponent mixtures in homogeneous, heterogeneous, and fractured porous media. With this numerical approach, we solve the unsteady-state convection/diffusion equations without adopting the Oberbeck-Boussinesq approximation. The diffusion coefficients and density are considered variables in space and time. We use the DG method to approximate the flow equations, which produces less numerical dispersion than the conventional upwind FD method. The MFE method is used to approximate the pressure unknown and the convective fluxes (velocity field). From our numerical experiments, we conclude that the MFE method in computing the convection fluxes has a high accuracy for systems having high contrast in permeability (10^7) or nonsmooth gridding. In contrast, the 2-point FD and FV approximations are not accurate enough to approximate the velocity field on unstructured grids even if the mesh is smooth.

To approximate the molecular diffusion fluxes, an alternative approach to the MFE method based on the LDG concept is implemented. The MFE and LDG methods are similar on the fact that both approximate the main unknown and its gradient simultaneously. The main difference between them is that the MFE method leads to a global system to calculate the fluxes, whereas, in the LDG method, the fluxes are calculated locally. Therefore, the LDG method is less costly from a numerical perspective. However, numerical comparisons show that the MFE is superior, especially for nonsmooth grids.

For fractured media, the discrete fracture model is implemented so that the fractures are treated as 1D entities. This approach reduces dramatically the CPU time because it avoids the complexities of the single-porosity model (eg, sharp spatial variations of parameters in matrix and fractures, refined gridding due to the length-scale difference between matrix and fractures).

ORCID

Hussein Hoteit http://orcid.org/0000-0002-3900-7272

REFERENCES

1. Oliveira Padua KG. Oil composition variation in a large deep water field. Paper presented at: SPE Latin American and Caribbean Petroleum Engineering Conference; 1997; Rio de Janeiro, Brazil.

2. Gupta DK, Lawrence J, Majid MNA, Wahlheim TA. Fluid characterization and modeling of compositional variation, Dukhan Field, Qatar. Paper presented at: SPE Conference: International Petroleum Technology Conference; 2009; Doha, Qatar.

3. Nasrabadi H, Firoozabadi A, Esposito RO, Vieira AJM. Interpretation of an unusual bubblepoint pressure variation in an offshore field. Paper presented at: SPE Conference: Europec/EAGE Conference and Exhibition; 2008; Rome, Italy.

4. Metcalfe RS, Vogel JL, Morris RW. Compositional gradients in the Anschutz Ranch East field. *SPE J*. 1988;3(3):1025-1032.

5. Hamoodi AN, Abed A, Grabenstetter J. Modeling of a large gas-capped reservoir with areal and vertical variation in composition. Paper presented at: SPE Conference: 69th Annual SPE Technical Conference and Exhibition; 1994; New Orleans, LA.

6. Lage JL, Nield DA. Convection induced by inclined gradients in a shallow porous medium layer. *J Porous Media*. 1998;1(1):57-69.

7. Thomas O. Reservoir Analysis Based on Compositional Gradients [PhD thesis]. Stanford, CA: Stanford University; 2007.

8. Nikpoor M. Modeling of Compositional Grading in Nonisothermal Petroleum Reservoirs [PhD thesis]. Calgary, AB: University of Calgary; 2014.

9. Ratulowski J, Fuex AN, Westrich JT, Sieler JJ. Theoretical and experimental investigation of isothermal compositional grading. *SPE Reserv Eval Eng*. 2003;6(3):168-175.

10. Montel F, Gouel PL. Prediction of compositional grading in a reservoir fluid column. Paper presented at: SPE Conference: SPE Annual Technical Conference and Exhibition; 1985; Las Vegas, NV.

11. Bolton EW, Firoozabadi A. Numerical modeling of temperature and SPEcies distributions in hydrocarbon reservoirs. *J Geophys Res-Earth Solid*. 2014;119(1):18-31.

12. Whitson CH, Belery P. Compositional gradients in petroleum reservoirs. Paper presented at: University of Tulsa Centennial Petroleum Engineering Symposium; 1994; Tulsa, OK.

13. Høier L, Whitson CH. Compositional grading—theory and practice. *SPE J*. 2001;4(6):525-535.

14. Jacqmin D. Interaction of natural convection and gravity segregation in oil/gas reservoirs. *SPE J*. 1990;5(2):233-238.

15. Riley MF, Firoozabadi A. Compositional variation in hydrocarbon reservoirs with natural convection and diffusion. *Aiche J*. 1998;44(2):452-464.

16. Ghorayeb K, Firoozabadi A. Modeling multicomponent diffusion and convection in porous media. *SPE J*. 2000;5(2):158-171.

17. Ghorayeb K, Firoozabadi A. Features of convection and diffusion in porous media for binary systems. *J Can Pet Technol*. 2001;40(2):21-28.

18. Ghorayeb K, Firoozabadi A. Numerical study of natural convection and diffusion in fractured porous medics. *SPE J*. 2000;5(1):12-20.

19. Hoteit H, Firoozabadi A. Multicomponent fluid flow by discontinuous Galerkin and mixed methods in unfractured and fractured media. *Water Resour Res*. 2005;41(11):1-15.

20. Hoteit H, Firoozabadi A. Compositional modeling of discrete-fractured media without transfer functions by the discontinuous Galerkin and mixed methods. *SPE J*. 2006;11(3):341-352.

21. Hoteit H, Firoozabadi A. Numerical modeling of diffusion in fractured media for gas-injection and -recycling schemes. *SPE J*. 2009;14(2):323-337.

22. Russell T, Wheeler MF. Finite element and finite difference methods for continuous flows in porous media. *The Mathematics of Reservoir Simulation*. Philadelphia, PA: SIAM; 1983:35-106.

23. Chavent G, Roberts JE. A unified physical presentation of mixed, mixed-hybrid finite-elements and standard finite-difference approximations for the determination of velocities in waterflow problems. *Adv Water Resour*. 1991;14(6):329-348.

24. Weiser A, Wheeler MF. On convergence of block-centered finite-differences for elliptic problems. *SIAM J Numer Anal*. 1988;25(2):351-375.

25. Arbogast T, Dawson CN, Keenan PT, Wheeler MF, Yotov I. Enhanced cell-centered finite differences for elliptic equations on general geometry. *SIAM J Sci Comput*. 1998;19(2):404-425.

26. Arbogast T, Wheeler MF, Yotov I. Mixed finite elements for elliptic problems with tensor coefficients as cell-centered finite differences. *SIAM J Numer Anal*. 1997;34(2):828-852.

27. Wheeler M, Xue GR, Yotov I. A multipoint flux mixed finite element method on distorted quadrilaterals and hexahedra. *Numer Math*. 2012;121(1):165-204.

28. Wheeler MF, Yotov I. A multipoint flux mixed finite element method. *SIAM J Numer Anal*. 2006;44(5):2082-2106.

29. Durlofsky LJ. Accuracy of mixed and control-volume finite-element approximations to Darcy velocity and related quantities. *Water Resour Res*. 1994;30(4):965-973.

30. Mose R, Siegel P, Ackerer P, Chavent G. Application of the mixed hybrid finite-element approximation in a groundwater-flow model-luxury or necessity. *Water Resour Res*. 1994;30(11):3001-3012.

31. Raviart P, Thomas J. *A Mixed Hybrid Finite Element Method for the Second Order Elliptic Problem*. New York, NY: Springer-Verlag; 1977.

32. Brezzi F, Fortin M. *Mixed and Hybrid Finite Element Method*. New York, NY: Springer-Verlag; 1991.

33. Yotov I. Mixed Finite Element Methods for Flow in Porous Media [PhD thesis]. Austin, TX: University of Texas; 1996.

34. Chavent G, Jaffre J. *Mathematical Models and Finite Elements for Reservoir Simulation*. North-Holland: Elsevier; 1986.

35. Sun SY, Wheeler MF. Discontinuous Galerkin methods for coupled flow and reactive transport problems. *Appl Numer Math*. 2005;52(2-3):273-298.

36. Girault V, Sun SY, Wheeler MF, Yotov I. Coupling discontinuous Galerkin and mixed finite element discretizations using mortar finite elements. *SIAM J Numer Anal*. 2008;46(2):949-979.

37. Kim M, Wheeler MF. Coupling discontinuous Galerkin discretizations using mortar finite elements for advection-diffusion-reaction problems. *Comput Math Appl*. 2014;67:181-198.

38. Cockburn B, Shu CW. The local discontinuous Galerkin method for time-dependent convection-diffusion systems. *SIAM J Numer Anal*. 1998;35(6):2440-2463.

39. Karimi-Fard M, Firoozabadi A. Numerical simulation of water injection in fractured media using the discrete-fracture model and the Galerkin method. *SPE Reserv Eval Eng*. 2003;6(2):117-126.

40. Karimi-Fard M, Durlofsky LJ, Aziz K. An efficient discrete-fracture model applicable for general-purpose reservoir simulators. *SPE J*. 2004;9(2):227-236.

41. Peng D, Robinson DB. A new two-constant equation of state. *Ind Eng Chem Fundam*. 1976;15(1):59-64.

42. Firoozabadi A. *Thermodynamics of Hydrocarbon Reservoirs*. New York, NY: McGraw-Hill; 1999.

43. Ghorayeb K, Firoozabadi A. Molecular, pressure, and thermal diffusion in nonideal multicomponent mixtures. *Aiche J*. 2000;46(5):883-891.

44. Firoozabadi A, Ghorayeb K, Shukla K. Theoretical model of thermal diffusion factors in multicomponent mixtures. *Aiche J*. 2000;46(5):892-900.

45. Hoteit H, Firoozabadi A. Compositional modeling by the combined discontinuous Galerkin and mixed methods. *SPE J*. 2006;11(1):19-34.

46. Hoteit H, Ackerer P, Mose R, Erhel J, Philippe B. New two-dimensional slope limiters for discontinuous Galerkin methods on arbitrary meshes. *Int J Numer Methods Eng*. 2004;61(14):2566-2593.

47. Fagherazzi S, Furbish DJ, Rasetarinera P, Hussaini MY. Application of the discontinuous SPEctral Galerkin method to groundwater flow. *Adv Water Resour*. 2004;27(2):129-140.

48. Noorishad J, Mehran M. An upstream finite-element method for solution of transient transport-equation in fractured porous-media. *Water Resour Res*. 1982;18(3):588-596.

49. Baca RG, Arnett RC, Langford DW. Modeling fluid-flow in fractured porous rock masses by finite-element Techniques. *Int J Numer Methods Fluids*. 1984;4(4):337-348.

APPENDIX

Modeling Fractures

A key step in the discrete fracture modeling is to represent 2D fracture cells with 1D elements, as shown in Figure A1. From the cross flow equilibrium concept,[19-21,45,48,49] the pressure in a fracture cell and the pressures in the neighboring matrix cells are assumed equal. By integrating the governing equations over the control volume that includes the fracture and the corresponding matrix cells alleviates the computation of the matrix-fracture fluxes. This technique is accurate and more efficient than the single porosity.
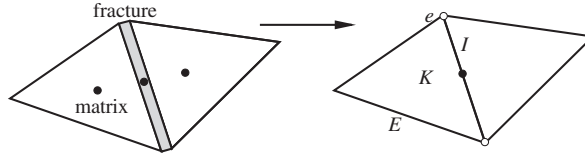
FIGURE A1   Geometric simplification of 2-dimensional fracture cells into 1-dimensional fracture cells

Let K be a grid block that contains a 1D fracture element I. By applying the mixed hybrid finite element formulation to Darcy's law over K, the flux $q_{K,E}$ across the edge E of K can be expressed as a function of the cell pressure average p_K and the edge pressure averages (pressure traces) $tp_{K,E}$, as shown in Equation 11. The same approach can be applied to discretized Darcy's law in the fracture element I. The flux $q_{I,e}$ across the extremity e of I can then be written as

$$q_{I,e} = \alpha_{I,e}p_I - \sum_{e' \in \partial I} \beta_{I,e,e'} tp_{I,e'} - \gamma_{I,e} \qquad e \in \partial I, \tag{A1}$$

where p_I and $tp_{I,e}$ are respectively the pressure average on I and the pressure traces at the extremities of I. In the grid cells that contain fractures, the block pressure average and the fracture slice average are equal, ie, $p_K = p_I$. By imposing the continuity of the fluxes, the flux unknown can then be eliminated and a linear system with the pressure average P and the pressure trace T_P is obtained, as in Equation 12.

The second step is to discretize the material balance equations. The integration of the second flow equation in Equation 6 over the matrix and fracture elements gives

$$\left(\int_K \phi \frac{\partial \varsigma_{K,i}}{\partial t} + \int_I \phi \frac{\partial \varsigma_{I,i}}{\partial t} \right) + \left(\int_K \varsigma_{K,i} \vartheta + \int_I \varsigma_{I,i} \vartheta \right) + \left(\int_K \nabla . \boldsymbol{J}_i + \int_I \nabla . \boldsymbol{J}_i \right) = 0, \quad i = 1, \ldots, n_c - 1. \tag{A2}$$

Using the divergence theorem (see Equation 8) and assuming that the average concentrations in the matrix and fracture cells are equal, Equation A2 simplifies to

$$(\phi_K |K| + |I|\phi_I) \frac{d\bar{\varsigma}_{i,K}}{dt} + \sum_{E \subset \partial K} q_{K,E} \, \tilde{\varsigma}_{K,E} + \varepsilon \sum_{e \subset \partial I} q_{I,e} \tilde{\varsigma}_{I,e} + \sum_{\partial K} f_i^{T,p,M} + \varepsilon \sum_{\partial I} f_i^{T,p,M} = 0, \tag{A3}$$

where $|K|$ and $|I|$ are respectively the volumes of matrix and fracture cells; ε is the fracture aperture; $\bar{\varsigma}_{i,K}$ is the cell averages of $\varsigma_{i,K}$; $\tilde{\varsigma}_{K,E}$ and $\tilde{\varsigma}_{I,e}$ are the concentrations from the upstream matrix and fracture cells, respectively; and $f_i^{T,p,M}$ represent the thermal, pressure, and molecular diffusion fluxes in the matrix and fractures. The expressions of these fluxes are given in Equations 18, 19, and 24. Note that the integration of the first equation in Equation 6 can be done similarly but without the diffusion term.